

Integrated device of luminescent solar concentrators and electrochromic supercapacitors for self-powered smart window and display

Received: 9 May 2024

Accepted: 19 February 2025

Published online: 01 March 2025

 Check for updates

Shichao Huang¹, Haotian Guo¹, Pengfei Xia¹, Hongcan Sun¹, Changgui Lu¹, Yuge Feng¹, Jing Zhu², Cai Liang³, Shuhong Xu¹✉ & Chunlei Wang¹✉

Luminescent solar concentrators are translucent photovoltaic modules potentially used for building window. To store the energy generated by them, a separate energy storage module and voltage regulator module are required, but it is clear that this pairing is unwieldy for application. To address this problem, we propose a “face-to-face” tandem integration of luminescent solar concentrators and electrochromic supercapacitors. In this case, the separated energy storage module and voltage regulator module are not required, since the electric energy produced by concentrators under sunlight can be directly stored by the supercapacitors with matched voltage window. The charged energy storage module can be used to supply low-power devices. Moreover, electrochromic supercapacitors exhibit adjustable average visible transmission under different energy storage state, making the integrated device interesting for self-powered electrochromic smart windows or display devices. As an example, a self-powered information instruction display is prepared, and text messages could be clearly and rapidly displayed in a controllable manner. The integrated device capable of photovoltaic conversion, energy storage, and electrochromism is a promising alternative for smart windows.

With the development of photovoltaics (PV) technologies, coping with the huge building energy consumption (30–40% of global energy consumption reported by International Energy Agency, IEA) doesn't seem to be a difficult task anymore^{1–3}. In order to realize zero emissions for buildings, besides laying opaque solar panels on the roof, photovoltaic conversion using the glass curtain wall on the side of the building has become a current research hotspot^{4–8}. As one type of translucent photovoltaic glass, luminescent solar concentrators (LSCs) are composed of luminophore-embedded transparent matrix with edge-coupled PV cells^{9,10}. Photons incident on the front sides of LSCs are absorbed and re-emitted by the luminophores, and then converged

to the edge-coupled PV cells through the waveguide, thus realizing photovoltaic conversion^{11–14}. Compared to solar cells, LSCs have an outstanding advantage, namely immune to the loss of power generation efficiency induced by the shadow effect, because of the nature of converting the luminescence of the luminophores rather than sunlight into electric energy by the edge PV cells. It is believed that LSCs are potential candidate for translucent glass curtain walls at the sides of buildings, especially in the case of urban buildings with the serious shadow effect^{15–17}. In this sense, translucent LSCs on the sides of buildings can be complemented with opaque solar cells on the roof, helpful for achieving the aim of zero emissions in buildings.

¹School of Electronic Science and Engineering, Southeast University, Nanjing, PR China. ²Chipown Micro-electronics limited, Wuxi, China. ³Key Laboratory of Energy Thermal Conversion and Control of Ministry of Education, School of Energy and Environment, Southeast University, Nanjing, China.

✉ e-mail: xush@seu.edu.cn; wangchl@seu.edu.cn

Since the output energy by LSCs is instant and unstable in different light environments, LSCs are usually required to connect with cumbersome solar energy management systems with both energy storage modules and voltage regulator module^{18–20}. For example, the solar energy management system was used for either LSCs-based self-powered temperature alarm devices or LSCs-based speed measurement devices^{21,22}. However, such solar energy management systems appear redundant and cumbersome for these reported devices. As for the application of photovoltaic glass, the connected solar energy management system may cause a series of problems, such as blocking the opening of sliding window, increasing the required space for installation, and not in line with architectural aesthetics^{23,24}. In this sense, it is highly desired to develop an integrated device between LSCs and translucent energy storage devices that is suitable for building windows. Up to now, it is still a research blank to assemble such an integrated device.

Electrochromic smart windows with reversible optical change for controlling indoor lighting by regulating the transmittance of sunlight have attracted great attentions^{25–28}. It is worth noting that previously reported electrochromic devices typically require an external power supply to drive the color-changing reaction, reducing the independence and flexibility of use as a smart window and resulting in additional energy consumption^{29–31}. To address this issue, different types of self-powered electrochromic smart windows have been proposed. One example is a self-powered smart window based on redox reactions. The redox reaction of a strongly reducing electrode with oxygen in the air produces a large electrode potential difference, which is used to drive the self-charging color change process of the device^{32,33}. However, the slow self-charging rate (the potential reaches 1.435 V in 10 min) and poor cycle life of such devices limit their use as architectural windows³⁴. Another example is the integration of translucent solar cells with electrochromic devices to prepare self-powered electrochromic systems^{35,36}. Besides the complex assembly process and high cost of translucent solar cells, the trade-off between the high average visible transmission (AVT) demand for windows and the high photoelectric conversion efficiency (PCE) requirement for solar cells is also a challenge. In particular, the translucent solar cells prepared by halide perovskites suffer from halogen segregation under the built-in electric field, resulting in a weak stability of device^{37–39}. In contrast, the all-optical operation mechanism (including sunlight absorption, fluorescence emission, and optical waveguide) of LSCs avoids the problem of halogen segregation and thus can substantially improve

the stability of devices. From this point, translucent LSCs potentially act as a stable candidate for architectural photovoltaics for self-powering electrochromic devices. Nevertheless, such self-powered electrochromic smart windows based on LSCs have not been reported yet.

In this work, we reported an integrated device of LSCs and electrochromic supercapacitors (ECs) in a manner of “face-to-face” tandem. Due to the integration of ECs, the cumbersome energy storage module can be avoided. Moreover, the ECs with a stable voltage window of 0–1.4 V can match the output voltage of the used LSCs (0–2.07 V), making it possible to avoid the voltage regulator module. As a result, solar management system is not required for LSCs-ECs integrated devices. After being charged by LSCs, the ECs can act as an energy storage module to supply low-power devices such as timers. In addition, the LSCs-ECs integrated device also shows reversible electrochromic behavior with changed AVT between 10.2% and 36.8% during the charging/discharging cycle of ECs. Due to the unique tri-functions of photovoltaic conversion, energy storage, and electrochromism, the LSCs-ECs integrated device can be used to build smart windows and information instruction displays. Compared to the combining devices between the separated solar cells and the separated ECs, the currently reported LSCs-ECs integrated devices inherit all the advantages of LSCs, making it possible to assemble integrated devices in a “face-to-face” manner.

Results and discussion

The “face to face” tandem LSCs-ECs integrated device in Fig. 1 consists of two components: (1) quasi-solid state ECs constructed by polyaniline (PANI) film electrode as the anodic electrochromic material and WO_3 film as the cathodic electrochromic material for both energy storage and electrochromism and (2) LSCs consisted of the red-emitting $\text{CsPbI}_3/\text{PMMA}$ composite with edge-coupled silicon solar cells for energy harvesting. In the following text, the performance of ECs, LSCs, and LSCs-ECs integrated devices is discussed in detail.

Quasi-solid state ECs for energy storage and electrochromism

To assemble quasi-solid state ECs, PANI and WO_3 electrodes were prepared on ITO by electrochemical deposition as confirmed by Fourier transform infrared spectroscopy (FTIR), X-ray diffraction (XRD) and X-ray photoelectron spectroscopy (XPS) results in Supplementary Fig. 1^{40–42}. After sandwiching the electrolyte of polyvinyl

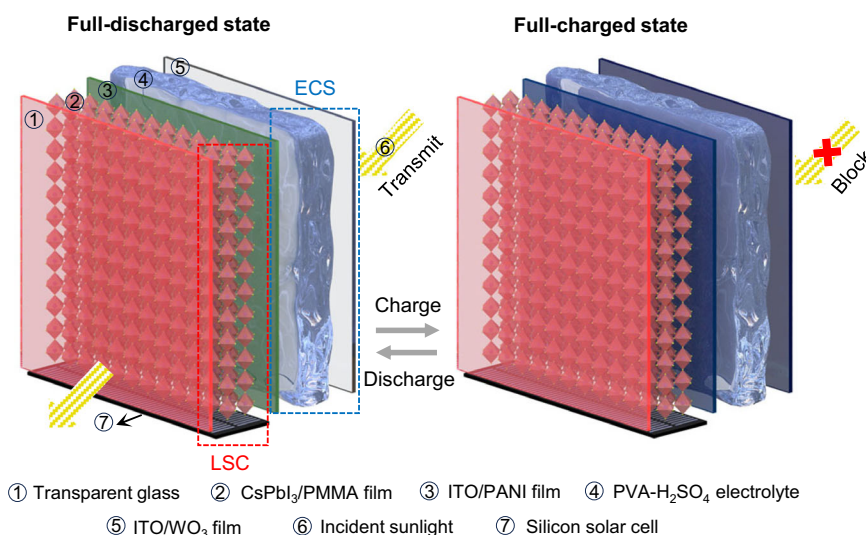


Fig. 1 | The diagram for the structure and modulation mechanism of the LSCs-ECs integrated device. Under solar irradiation, the electrical energy generated by the LSCs will be stored in the ECs, while causing a decrease in the transmittance of the ECs to block light incidence.

alcohol (PVA)-sulfuric acid (H_2SO_4), a $5 \times 5 \text{ cm}^2$ ECS was assembled as illustrated in Supplementary Fig. 2.

To optimize the performance of PANI electrodes, PANI films of different thicknesses were prepared by adjusting the electrodeposition time. According to the cyclic voltammetry (CV) curve in Supplementary Fig. 3, galvanostatic charge-discharge (GCD) curve in Supplementary Fig. 4, and electrochemical impedance spectroscopy (EIS) in Supplementary Fig. 5, the PANI electrode with an electrodeposition time of 600 s exhibited high specific capacity (13.8 mF cm^{-2} at a current density of 0.1 mA cm^{-2} calculated by Eq. 1 in Supplementary Information) and excellent electrochemical behavior, thus it was selected for the next step of the study^{43,44}. Similarly, we also optimized the WO_3 electrode by controlling the deposition time. By comparing the CV in Supplementary Fig. 6a, GCD in Supplementary Fig. 6b, and EIS in Supplementary Fig. 7 of WO_3 electrodes with different electrodeposition times, WO_3 -45 with a high specific capacity up to 46.8 mF cm^{-2} at 0.5 mA cm^{-2} in Supplementary Fig. 8 was selected as the counter electrode of PANI-600 due to their almost equal integral areas of CV curves in Supplementary Fig. 6c. In this case, both electrodes can store almost the same amount of electric quantity.

The electrochemical performance for a quasi-solid state PANI-600/ WO_3 -45 ECSs was tested. (1) From the CV curves in Fig. 2a, the electrochemical performance of the ECSs remains stable under the large electrochemical window (0–1.4 V). Among them, the pair of redox peaks 1.28 V/1.2 V belongs to WO_3 . The left two pairs of distinct redox peaks were observed at 0.67 V/0.6 V and 0.8 V/0.75 V on the low-rate scanning curves, corresponding to the reaction process of PANI. It should be emphasized that the stable voltage window of 0–1.4 V for PANI-600/ WO_3 -45 ECSs can match the output voltage of the PV cell on the side of LSCs according to Supplementary Table 1. As a result, the use of voltage regulation modules can be avoided. (2) From the GCD results in Fig. 2b, the charging and discharging processes exhibit nonlinearity at different current densities from 0.1 mA cm^{-2} to 2 mA cm^{-2} due to the fact that the form of energy storage belongs to Faraday pseudocapacitor storage rather than the double layer

capacitor storage^{45,46}. The specific area capacitance and mass capacitance (calculated by Eq. 2 in Supplementary Information) of the PANI-600/ WO_3 -45 ECSs was calculated from the discharge curve as 8.57 mF cm^{-2} and 12.2 F g^{-1} at a current density of 0.1 mA cm^{-2} , respectively. In Fig. 2c, the specific area capacitance of ECSs shows a corresponding decrease in the high discharge current, which is related to the nature of the supercapacitor itself⁴⁷. Further, the energy density and power density in Fig. 2c, which are important parameters of PANI-600/ WO_3 -45 ECSs, were calculated by Eq. 3 and 4 in Supplementary Information as 23.3 mW h m^{-2} and 0.7 mW m^{-2} at a current density of 0.1 mA cm^{-2} , respectively^{40,48}. In the inserted image of Fig. 2a, c single device is enough to light up a timer, indicating the potential applications of the ECSs in the field of energy supply. (3) From the fitting and simulation result of EIS in Supplementary Fig. 9, the PANI-600/ WO_3 -45 ECSs clearly exhibited a small charge transfer resistance of $\sim 2.5 \Omega$ (the semicircle diameters in the mid-frequency part), facilitating the rapid redox reaction on electrode^{49,50}. In addition, the Warburg impedance (between mid- and low-frequency part) of the PANI-600/ WO_3 -45 ECSs indicates an obvious ions diffusion behavior in WO_3 -45^{51,52}. The straight lines with larger slope in the low-frequency part describe rapid ion transport during the electrochemical processes, corresponding to the high ionic conductivity (up to 285.5 mS cm^{-1}) of the PVA- H_2SO_4 electrolyte as shown in Supplementary Table 2⁵³.

Beside energy storage, PANI-600/ WO_3 -45 ECSs exhibit an adjusted AVT (calculated by Eq. 5 in Supplementary Information) during charging/discharging process, due to the matching electrochromic behavior of PANI and WO_3 . In Fig. 2d, the transmission of both PANI and WO_3 electrodes decreases/increases during the charging/discharging process of ECSs, resulting in the color change from light green to dark blue. According to Supplementary Fig. 10 and 11, the PANI-600 and WO_3 -45 electrodes deliver a good light modulation ability in the visible light region and the coloration efficiency of $182.5 \text{ cm}^2 \text{ C}^{-1}$ and $73.8 \text{ cm}^2 \text{ C}^{-1}$ at 700 nm, respectively. At the voltage of 0 V (namely the state of full-discharging), the PANI-600/ WO_3 -45 ECSs exhibit an AVT of 49% from 400 to 780 nm with a light green color

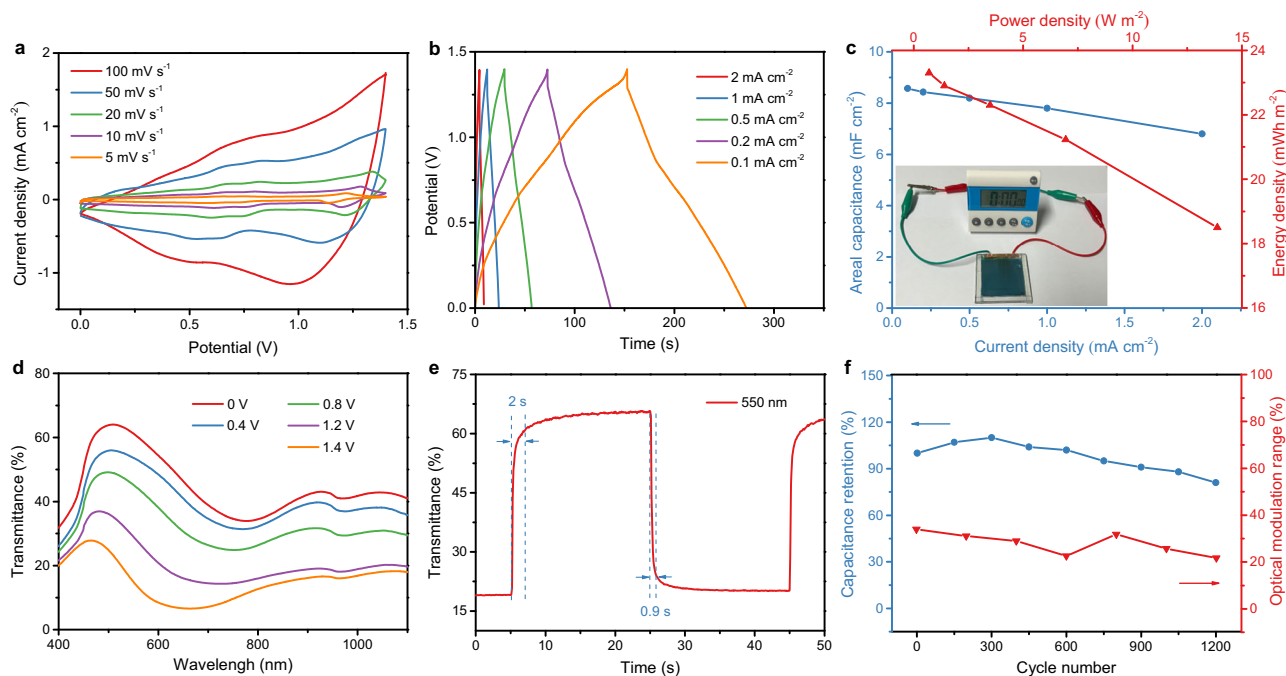


Fig. 2 | The performance of PANI-600/ WO_3 -45 ECSs. a CV curves at different scan rates under 0–1.4 V voltage window. **b** GCD curves at different current densities. **c** Ragone plot and the areal capacitance at different current densities. Inset: Optical image shows a ECSs was enough to light up a timer. **d** Transmittance spectra at 0 V,

0.4 V, 0.8 V, 1.2 V, and 1.4 V. **e** Real-time transmittance changes during reversible switching measured at 550 nm. **f** Capacitance and electrochromic stability in the visible region at current density of 1 mA cm^{-2} for 1200 cycles. Source data are provided as a Source Data file.

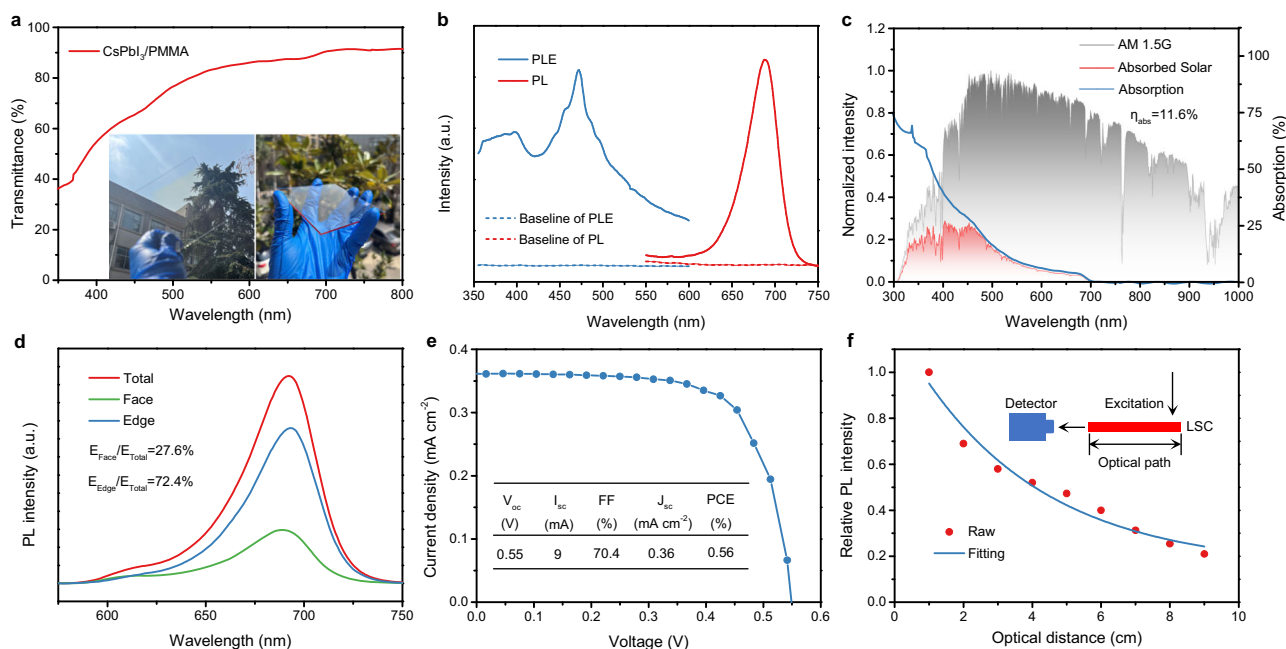


Fig. 3 | The performance of LSCs. a Transmittance of CsPbI₃/PMMA composite films. Inset: photographs of CsPbI₃/PMMA composite films with glass substrate in ambient light. **b** Photoluminescence (PL) and photoluminescence excitation (PLE) spectra of the CsPbI₃/PMMA composite films. The baseline was measured by using a transparent glass. **c** Absorption curves of CsPbI₃/PMMA composite films, and the standard solar spectrum AM 1.5 G. **d** Front and side emission of LSCs. **e** The *J*-*V* curve

of the PV cell coupled with the edges of LSCs under the 1 sun condition. V_{oc} , I_{sc} , *FF*, and J_{sc} are the open-circuit voltage, the short-circuit current, the fill factor, and the short-circuit current density, respectively. **f** PL intensity of CsPbI₃/PMMA LSCs with different optical paths. Inset: schematic of PL intensity measurement with different optical paths. Source data are provided as a Source Data file.

induced by the PANI electrode in the reduced state. As the voltage rises, the transparent WO₃ electrode and the PANI electrode undergo a synergistic redox reaction, and the color of the device gradually deepens. At the voltage of 1.4 V, the dark blue PANI-600/WO₃-45 ECSs have an AVT of only 14%. In Fig. 2e, the real-time transmittance curve measured at 550 nm reveals that PANI-600/WO₃-45 ECSs deliver a faster coloration time and bleaching time of 0.9 s and 2 s, respectively. It shows the rapid response rate of ECSs. Moreover, the PANI-600/WO₃-45 ECSs also show a certain light modulation ability in short-wave infrared (SWIR) regions (780–1100 nm), reaching an integrated optical transmittance of 41% and 16% at 0 V and 1.4 V, respectively.

From the long cycle test result in Fig. 2f and Supplementary Fig. 12, the PANI-600/WO₃-45 device exhibits capacitance retention of 82% after 1200 cycles of charging and discharging at a current density of 1 mA cm⁻². In particular, the specific capacitance of the ECSs increases after 200–300 cycles, due to the in-situ activation of the electrodes caused by diffusion of electrolyte^{54,55}. In terms of electrochromic stability in Fig. 2f and Supplementary Fig. 13, the optical modulation range, which is defined as the difference for the average transmittance in the visible region between 1.4 V charging state and 0 V discharging state, shows an overall decreasing trend from 34.1% before cycling to 22% after 1200 charge/discharge cycles, together with prolonged response time in Supplementary Fig. 14. Moreover, the transmittance spectrum of ECSs appears a new peak around 700 nm after 800 cycles, which leads to increased trend of optical modulation range during 800 cycles and 1000 cycles. Such new peak is probably caused by the detachment of the electrode material according to the scanning electron microscope (SEM) and XPS results in Supplementary Fig. 15, which is commonly reported due to the volume expansion and contraction of the electrode film⁵⁶.

It should be emphasized that the injected/ejected charge balance between the two electrodes is crucial for the performance of ECSs. In validation experiments, we purposely prepared WO₃ electrodes with a lower specific capacitance of 9.7 mF cm⁻² via spin-coating technique

(marked as WO₃-S) in Supplementary Fig. 16. Such electrode prepared by spin-coating technique is difficult to match with PANI-600 for maintaining the injected/ejected charge balance during the redox reaction. Though the assembled PANI-600/WO₃-S ECSs show the adjustable AVT from 58% (0 V) to 17% (1.4 V) during the charging/discharging process, it is also observed the small reaction current and ignorable redox peaks of WO₃ in the CV curves, low specific capacitance of 3.6 mF cm⁻², low energy density of 9.88 mWh m⁻² and larger charge transfer resistance of -7Ω (Supplementary Fig. 17a–e). In addition, the capacitive performance of the PANI-600/WO₃-S ECSs decreased to 77% after 1100 cycles in Supplementary Fig. 17f. Obviously, the ECSs assembled by mismatched positive and negative electrodes exhibit poor electrochemical capacity. According to the reference, supercapacitors assembled with mismatched positive and negative electrodes are not only difficult to maximize performance but also produce over-discharge phenomena. Under such a deep discharge process, the electrode materials are often damaged seriously affecting the stability of the device^{57,58}.

The self-powered LSCs-ECSs integrated devices

Before the assembling of the LSCs-ECSs integrated device, a red light emitting LSCs was first prepared via in situ blade coating on a glass substrate (Supplementary Fig. 18) for photon collection using ligand-modified CsPbI₃ nanocrystals and PMMA as luminophores and luminescent layer matrix, respectively. XRD in Supplementary Fig. 19a and energy dispersive spectroscopy in Supplementary Fig. 19b indicate the uniformly distributed cubic phase CsPbI₃ nanocrystals in PMMA^{59–61}. As-prepared CsPbI₃/PMMA composite films exhibit a high AVT of 80% in Fig. 3a, red-emission peak around 688 nm at the optimum excitation wavelength of 470 nm in Fig. 3b, and the absolute photoluminescence quantum yield (PLQY) of 54.9% as tested in the integrating sphere in Supplementary Fig. 20⁶². According to Fig. 3c, d, the absorption efficiency (η_{abs}), edge-emission efficiency (η_{edge}), and internal optical efficiency (η_{int}) are calculated as 11.6%, 72.4%, and 39.8% by Eq. 6 in

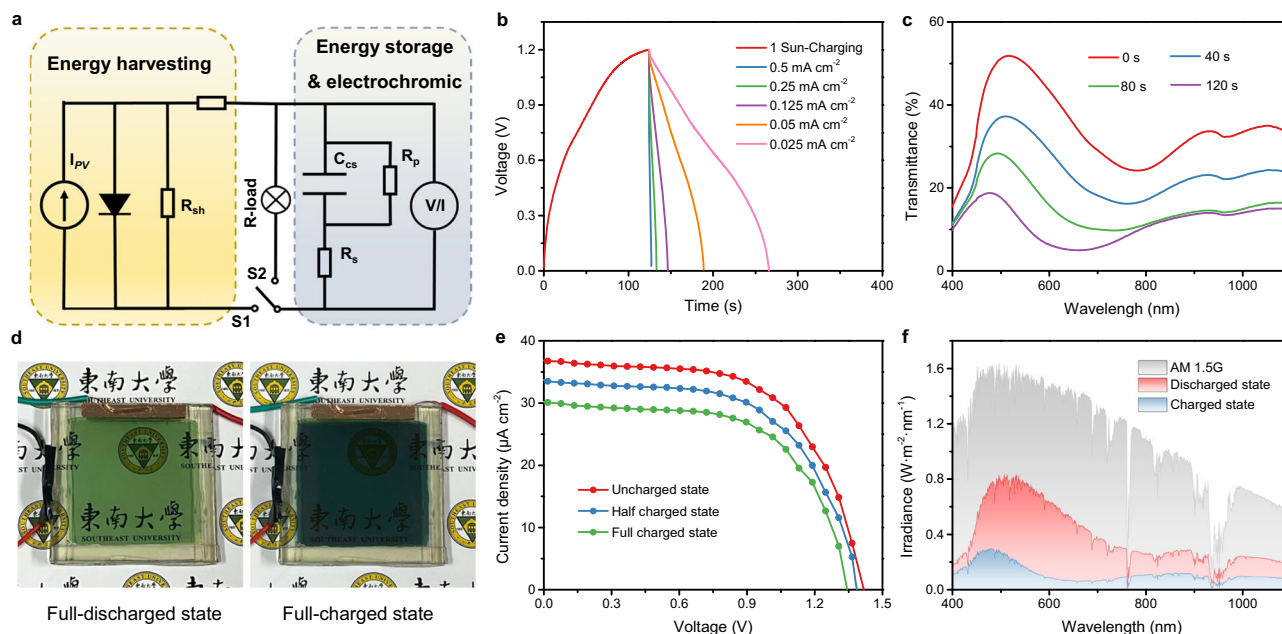


Fig. 4 | Performance of LSCs-ECSs integrated device. **a** Electric circuit diagram of device. **b** The V - t curves of integrated device during charging process under the 1 sun condition and discharging process under dark environment at different current densities. **c** Transmittance spectra of integrated device at different charging time under the 1 sun condition. **d** Photographs of integrated device under full-

discharged state and full-charged state. **e** J - V curves of integrated device with different charging state under the 1 sun condition. **f** Solar irradiance spectra of integrated device at charging/discharging state states. Source data are provided as a Source Data file.

Supplementary Information. Thus, the resulting external optical efficiency (η_{ext}) of LSCs is 4.6% (calculated by Eq. 7 in Supplementary Information)⁶³, which is higher than that of most reported LSCs in Supplementary Table 3. From the current density-voltage (J - V) curve of LSCs in Fig. 3e, the PCE and light utilization efficiency (LUE) values of the $5 \times 5 \text{ cm}^2$ device under the 1 sun condition are calculated as 0.56% and 0.45% by the Eq. 8 in Supplementary Information and Supplementary Table 4^{64–66}. The integrated short-circuit current density (J_{sc}) obtained by testing the average position-dependent external quantum efficiency ($\text{EQE}_{\text{LSC}}(\lambda)$) of the LSCs in Supplementary Fig. 21 corresponds to the J_{sc} value extracted from the J - V curve. In addition, the light intensity of the composite film can still reach 21% of the initial light intensity at a light path length of 9 cm in Fig. 3f. After one month of storage in ambient air (temperature: 298 K, relative humidity: 35%) in Supplementary Fig. 22, the PLQY and PCE of the device can still maintain 85% and 81%, indicating that the PMMA polymer has a certain protective effect on CsPbI_3 nanocrystals.

For assembling the LSCs-ECSs integrated device, PANI-600/ WO_3 -45 ECSs and LSCs with both working areas of $5 \times 5 \text{ cm}^2$ were assembled together via UV curing agent following by series connection PV cell to electrodes of ECSs. The two switches were connected to the circuit as shown in Fig. 4a. As a result, ECSs were charged/discharged by LSCs/R-load in the case of turning on the S_1/S_2 switch. First, the charging process by turning on the S_1 switch was measured. In this process, the light energy collected by the LSCs is converted into electrical energy and stored in the ECSs. (1) We studied the charging time of the LSCs-ECSs integrated device in different environments. In the case of 1 sun, the integrated device was successfully charged to 1.2 V in 124 s, as shown in the charging curve in Fig. 4b and Supplementary Movie 1. The integrated devices show moderate self-powered efficiency and capacitance stability but a relatively short charging time for achieving relative high voltage compared with different types of self-charging devices (Supplementary Table 5). In the case of low light environment, it requires 400 s when the device is charged to 0.45 V in Supplementary Fig. 23 under the LED illumination (8 W, 6500 K, 800 lm, Warm White). (2) In the charging process, the transmittance and color of the

device were changed due to the oxidation of PANI and reduction of WO_3 . From Fig. 4c, the AVT of the LSCs-ECSs integrated device change from 36.8%, 25%, 16.7% to 10.2% at the charging time from 0 s, 40 s, 80 s to 120 s, along with obvious color changes from light green to dark blue as shown in Fig. 4d. In SWIR regions, the device achieves the integrated optical transmittance of 31.4% in the discharged state, which decreases to only 13.4% after 120 s of charging. (3) The decreased transmittance of ECSs during the charging process can also lead to the decreased output power of LSCs due to the decreased amounts of photons received by the LSCs. As shown in J - V curves of Fig. 4e, a slight drop in both open circuit voltage and short circuit current density can be seen and the PCE values of LSCs were 0.13%, 0.12%, and 0.1%, respectively, when the ECSs is charged to 0 V, 0.6 V and 1.2 V. Similar results were also observed during the charging process in low light environment under the LED illumination in Supplementary Fig. 24. Second, the ECSs was discharged by R-load when the S_2 switch was turned on. Based on this discharge curve in Fig. 4b, the area capacitance of the device in Supplementary Table 6 was calculated to be 0.96–2.94 mF cm^{-2} in the current density range of 0.5–0.025 mA cm^{-2} . It may satisfy energy requirement of some low-power devices such as timer as shown in Fig. 2c.

The application of self-powered LSCs-ECSs integrated device

Being of the trifunctions of photovoltaic conversion, energy storage, and electrochromism, the LSCs-ECSs integrated devices can be used in many fields. First, since the ECSs achieve an energy density of 23.3 mWh m^{-2} as we have discussed above, the charged LSCs-ECSs integrated devices can act as an energy storage device to continuously supply for low-power devices, such as a timer in Fig. 2c and Supplementary Movie 2.

Second, LSCs-ECSs integrated devices can act as quick-convertible smart window for building or automobile by replacing traditional windows. If needing a light/dark environment, the switch S_2/S_1 can be turned on. Then the device can quickly discharge/charging, realizing the state change of the smart window between blackout and light transmission. Considering that the integrated device is

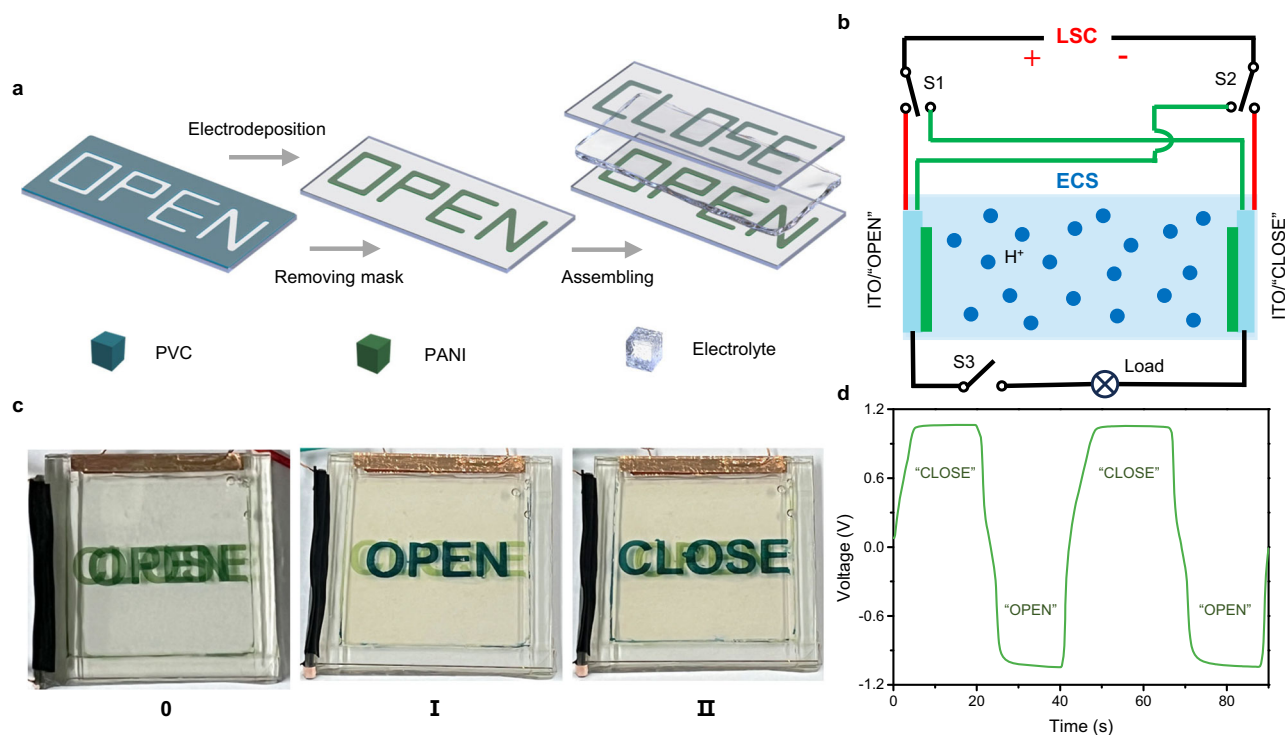


Fig. 5 | The self-powered display based on the LSCs-ECSs integrated device.

a Schematic illustration of the fabrication process of electrochromic display. Polyvinyl chloride (PVC) sticker is used as a mask. **b** An equivalent circuit of the self-powered display. S1 and S2 are connected to the red or green wires simultaneously to realize the switching of on gear “I” or “II”, respectively. When S3 is individually

switched on, the device is in gear “0”. **c** The optical photographs of the self-powered display in three different states of switch. **d** The V - t curves of the self-powered display under 1 sun condition. Source data are provided as a Source Data file.

capable of modulating visible and SWIR light, the solar irradiation transmittance in the full-charged or full-discharged state was calculated to evaluate the actual irradiation modulation in Fig. 4f. In the discharged state, the integrated device blocks 69.4% of the near-infrared radiation as well as maintaining 38% transmittance in the visible region; while the integrated device in the charged state blocks 86.9% of the solar radiation in the short wave near-infrared region, hence it is possible to control the light and heat entering into building or automobile by the smart window.

Third, the LSCs-ECSs integrated device can be also applied as a self-powered display. Herein, a layer of PANI with a pattern of “OPEN”, PVA- H_2SO_4 electrolyte, and another layer of PANI with a pattern of “CLOSE” were used to assemble ECSs in Fig. 5a. To enable fast switching between “OPEN” and “CLOSE”, a three-gear control switch is introduced into the circuit as shown in the equivalent circuit diagram (Fig. 5b). At the charging voltage of 1 V by LSCs under 1 sun condition, the ECSs were displaying a different message in a different state of the switch. (1) When the switch is placed on the gear “0”, the connection of LSCs and ECSs was broken. In this situation, both “OPEN” and “CLOSE” appear in green color, making it impossible to clearly communicate a clear text message (Fig. 5c). (2) When the switch is switched to gear “I”, the bottom pattern “OPEN” rapidly changes to dark blue due to the oxidation of PANI, making it easy to be observed. In comparison, the top pattern “CLOSE” changes to undertint green, which is not easy to observe. As a result, a distinct “OPEN” was displayed. (3) During the transition from gear “I” to gear “II”, the device is rapidly discharged and then recharged in reverse, resulting in a clear display of the “CLOSE” text message. The complete operational sequence of the self-powered display device is captured in Supplementary Movie 3. The device is capable of charging to 1.1 V within 2 s for fast display of text messages as shown in the V - t curve of Fig. 5d. In addition, the device can be discharged into standby mode within 2 s with the assistance of a series

resistor. Similar results were also observed in low light environment under the ambient LED illumination (8 W, 6500 K, 800 lm, Warm White). The display is still able to charge quickly to more than 0.5 V under the LED illumination and convey clear information as shown in Supplementary Fig. 25 and Supplementary Movie 4.

In conclusion, we demonstrated a trifunctional LSCs-ECSs integrated device with photovoltaic conversion, energy storage, and electrochromism by connecting LSCs and ECSs in series via a “face-to-face” approach. This self-powered integrated device achieves an area capacitance of 2.94 mF cm^{-2} and can be quickly charged to 1.2 V within 124 s under 1 sun condition for supplying low-power devices. Moreover, the integrated device has reversible electrochromic behavior (AVT between 10.2% and 36.8%). Based on the color-changing nature of the integrated device, we have prepared self-powered displays that can rapidly display textual information within 2 s. However, the current LSCs-ECSs integrated device still has the small energy density, which is far from the requirement of practical energy storage product. The possible solution in future includes using high specific capacity materials as electrodes, doping the electrolyte with multivalent ions, broadening the operating voltage window, and integration of ions batteries as alternative energy storage modules. Moreover, the cycling stability of LSCs-ECSs integrated device still needs to be further improved before practical application. The possible solution in future includes the developing of novel electrochromic materials with better stability and introducing hierarchical porous electrode scaffold for loading the electrochromic materials to reduce the structural damage caused by lattice volume changes.

Methods

Materials

Octylammonium iodide (OAI, >99.5%), lead iodide (PbI_2 , 99.99%), and Cesium Iodide (CsI, 99.9%) were purchased from Xi’an Polymer Light

Technology Corp. Polymethyl methacrylate (PMMA) was purchased from Sinopharm. N, N-dimethylformamide (DMF, AR) was purchased from Nanjing Reagent. UV-curable adhesive (K2018) was purchased from KSIMI. Ethanol (CH₃CH₂OH), Sulfuric acid (H₂SO₄), hydrogen peroxide (H₂O₂), Sodium tungstate dihydrate (Na₂WO₄), Acetic acid (CH₃COOH) and Acetone (CH₃COCH₃) were purchased from Sinopharm Chemical Reagent Co. Ltd. Tungsten hexachloride (WCl₆, 99.5%) was purchased from Macklin Reagent Co. Ltd. Aniline and Poly (vinyl alcohol) 1799 (PVA) were purchased from Aladdin Shanghai Aladdin Biochemical Technology Co., Ltd. All materials were used without further purification. Si-PV was purchased from Telesky International Limited. The indium tin oxide (ITO) substrates (8 Ω sq⁻¹) were purchased from Luoyang Guluo Glass Co., Ltd (China).

Fabrication of electrodeposited PANI film

In a typical synthesis, the ITO glass was washed with acetone, ethanol, and deionized (DI) water successively and dried. In a three-electrode system (Ag/AgCl as the reference electrode and Pt foil as the counter electrode), ITO glass was immersed into the electroplating precursors (0.05 M aniline, 1 M H₂SO₄) and applied a voltage of 1 V for different electrodeposition time of 300 s, 450 s, 600 s, 750 s, and 900 s. The above PANI electrodes are named PANI-300, PANI-450, PANI-600, PANI-750, and PANI-900 based on the deposition time.

Fabrication of electrodeposited WO₃ film

First, 0.1M Na₂WO₄ was dissolved in water at 60 °C with constant stirring, and then 0.08 M H₂O₂ and 0.36 M H₂SO₄ were added slowly and sequentially. After stirring for 5 min, a yellow electroplating solution of WO₃ was obtained. Then, in a three-electrode system (Ag/AgCl as the reference electrode and Pt foil as the counter electrode), ITO glass was immersed into the electroplating solution and applied a voltage of -0.5 V for different electrodeposition time of 15 s, 30 s, 45 s, and 60 s. The above WO₃ electrodes are named WO₃-15, WO₃-30, WO₃-45, and WO₃-60 based on the deposition time.

Fabrication of spin-coated WO₃ film

The WO₃ films were prepared by the sol-gel spin-coating techniques. 0.5 g of WCl₆ powder was dissolved in 10 ml of anhydrous ethanol and 1 ml of glacial acetic acid was added to the mixed solution. The solution was then stirred at room temperature for 30 min, and 1 ml of H₂O₂ was added to the mixed solution and further stirred for 30 min. Subsequently, the resulting light green color solution was stirred at 40 °C until a homogeneous and transparent solution was obtained. The resulting solution was then spin-coated onto the treated ITO substrate at 2000 rpm and subjected to solvent evaporation at 100 °C. Finally, the electrodes were annealed by holding at 250 °C for 2 h in a tube furnace. The spin-coated WO₃ are named WO₃-S.

Quasi-solid state ECSs assembly

The ECSs were assembled using two pieces of ITO glass with PANI or WO₃ film. 3M™VHB™ tape was used to seal three sides of the device. Then, the PVA-H₂SO₄ electrolyte was injected into the device by a syringe through the unsealed side.

Fabrication of CsPbI₃/PMMA LSCs

0.027 mmol CsI, 0.027 mmol PbI₂, and 0.019 mmol Octylammonium iodide (C₈H₂₀NI, OAI) were dissolved in 10 mL DMF under magnetic stirring. Then, PMMA (0.9 g) was dispersed into the above solution. The mixture was kept stirring for 24 h at room temperature to form the viscous slurry. After that, the precursor slurry was blade-coated onto the clean glass to obtain a uniform film. The obtained glass substrate was transferred into heating plate and maintained at 130 °C for 5 min for the crystallization of OA-modified CsPbI₃ nanocrystals.

Fabrication of LSCs-ECSs integrated devices

A glass with a CsPbI₃/PMMA composite film is directly affixed to the backside of the electrodes of the ECSs by using a UV-curable adhesive, where the CsPbI₃/PMMA composite film is sandwiched in the center. Then, the samples were irradiated with a UV lamp (365 nm) for curing. Finally, the PV cells (the specific performance parameters as shown in Supplementary Table 1) are attached to the edges of the above structure, and their exposed light-absorbing parts are wrapped in black tape so as not to interfere with the optoelectronic testing of the integrated device.

Fabrication of ECSs for display

A PVC sticker is applied as a template to the conductive side of the ITO, and the desired PANI pattern is generated in the exposed area by electrodeposition. After separating the stickers, the resulting patterned PANI electrodes were symmetrically assembled on both sides of the gel electrolyte to form the ECS (electrochromic display section). Two commercial monocrystalline silicon cells with an open-circuit voltage of 0.69 V and a short-circuit current of 58 mA (the specific performance parameters in Supplementary Table 7) were connected in series, and then coupled to one side of the LSCs, and their exposed portions were taped with black tape. The other parts are the same as the LSCs-ECSs integrated device preparation process described above. Finally, a three-gear transfer switch is used to connect the entire circuit.

Characterizations

XRD investigation was carried out by using the Bruker D8 advance with monochromatized Cu Kα radiation (λ = 1.5418 Å). XPS was measured by Thermo Scientific Escalab 250Xi. FTIR was implemented by Bruker Vertex80v. The energy dispersive X-ray spectroscopy and SEM images were measured by FEI Quanta FEG 250.

Electrochemical test

The electrochemical test of the ECSs was carried out by the electrochemical workstation (CHI660D, Shanghai, China). The ionic conductivity of PVA-H₂SO₄ electrolyte was tested using an ionic conductivity meter (DZB-712F). The in situ transmittance spectra and response times were recorded from a Shimadzu 3600 UV-vis near-infrared spectrophotometer coupled with the electrochemical workstation. The masses of the PANI-600 and WO₃-45 films obtained by cumulative weighing method were 0.5 mg cm⁻² and 0.2 mg cm⁻², respectively. Transmittance was recorded with Shimadzu 3600 UV-vis near-infrared spectrophotometer. Coloration efficiency of ECSs was calculated from the following formulae: CE = ΔOD/(Q/A); ΔOD = log (T_b/T_c), where Q/A is the injected charge Q per unit electrode area A. T_b and T_c are the transmittances of the films in their bleached and colored states at the specified wavelengths, respectively. The response times were defined as the times required for 90% of change in the full optical modulation at the specified wavelengths.

Optoelectronic test

Photoluminescence (PL) and photoluminescence excitation (PLE) spectra were recorded with a Shimadzu RF-5301 PC spectrofluorometer, and the excitation wavelength was set as 470 nm. The PLQYs of CsPbI₃/PMMA composite films were measured by Edinburgh F55 with the excitation wavelength at 470 nm at room temperature. The EQE of LSCs was measured on Enlitech QE-R. For the edge efficiency of the LSCs, the total emission from the LSCs was first tested with an integrating sphere, and then the emission from the surface of the LSCs was measured by masking the four edges of the LSCs with black tape. The difference between the total emission and the surface emission is the edge emission. The edge efficiency values of the LSCs were obtained by calculating the integral area of the three curves. The absorbance (A = 1 - 10^{-OD}, blue line) was convolved with the normalized

AM1.5 solar spectrum. The ratio of the obtained solar absorption integral area to the normalized solar spectrum is the absorption efficiency of the LSCs. The properties of the Si cells used for the performance testing of LSCs were as follows, V_{oc} of 0.6 V, I_{sc} of 0.076 A, fill factor of 70.3%, J_{sc} of 38 mA cm⁻², PCE value of 16.5%. I - V curves were measured by solar simulator (model 66902) from Newport, which had a 300 W Xenon lamp with an irradiance of 100 mW cm⁻² (AM 1.5 G). The LED lamp was purchased from Philips (CorePro E27 LED GLS Bulb 8 W, 6400 K, 800 lm, Warm White).

Data availability

The authors declare that the data supporting the findings of this study are available within the article and its Supplementary Information. Extra data are available from the corresponding authors upon request. Source data are provided with this paper.

References

1. Yu, G., Yang, H., Luo, D., Cheng, X. & Ansah, M. K. A review on developments and researches of building integrated photovoltaic (BIPV) windows and shading blinds. *Renew. Sust. Energy Rev.* **149**, 11355 (2021).
2. Liu, H. et al. Building integrated concentrating photovoltaic window coupling luminescent solar concentrator and thermotropic material. *Energy* **284**, 129237 (2023).
3. Li, Y., Huang, X., Sheriff, H. K. M. & Forrest, S. R. Semitransparent organic photovoltaics for building-integrated photovoltaic applications. *Nat. Rev. Mater.* **8**, 186–201 (2022).
4. Cuce, E. Toward multi-functional PV glazing technologies in low/zero carbon buildings: heat insulation solar glass-latest developments and future prospects. *Renew. Sust. Energy Rev.* **60**, 1286–1301 (2016).
5. Wagner, L., Mastroianni, S. & Hinsch, A. Reverse manufacturing enables perovskite photovoltaics to reach the carbon footprint limit of a glass substrate. *Joule* **4**, 882–901 (2020).
6. Domjan, S., Arkar, C., Begelj, Ž. & Medved, S. Evolution of all-glass nearly zero energy buildings with respect to the local climate and free-cooling techniques. *Build. Environ.* **160**, 106183 (2019).
7. Pinheiro, D. et al. NIR-emitting electrochromic windows for cold climate region buildings. *ChemElectroChem* **11**, e202300479 (2023).
8. Correia, S. F. H. et al. Bio-based solar energy harvesting for onsite mobile optical temperature sensing in smart cities. *Adv. Sci.* **9**, e2104801 (2022).
9. Mateen, F., Oh, H., Kang, J., Lee, S. Y. & Hong, S.-K. Improvement in the performance of luminescent solar concentrator using array of cylindrical optical fibers. *Renew. Energy* **138**, 691–696 (2019).
10. Zhou, Y. et al. Near infrared, highly efficient luminescent solar concentrators. *Adv. Energy Mater.* **6**, 1501913 (2016).
11. Debije, M. G. & Verbunt, P. P. C. Thirty years of luminescent solar concentrator research: solar energy for the built environment. *Adv. Energy Mater.* **2**, 12–35 (2011).
12. Tong, J. et al. Fabrication of highly emissive and highly stable perovskite nanocrystal-polymer slabs for luminescent solar concentrators. *J. Mater. Chem. A* **7**, 4872–4880 (2019).
13. Nikolaidou, K. et al. Hybrid perovskite thin films as highly efficient luminescent solar concentrators. *Adv. Opt. Mater.* **4**, 2126–2132 (2016).
14. Zhou, N. et al. A review of perovskite nanocrystal applications in luminescent solar concentrators. *Adv. Opt. Mater.* **11**, 2202681 (2023).
15. Debije, M. G. & Rajkumar, V. A. Direct versus indirect illumination of a prototype luminescent solar concentrator. *Sol. Energy* **122**, 334–340 (2015).
16. Corsini, F. et al. Highly emissive fluorescent silica-based core/shell nanoparticles for efficient and stable luminescent solar concentrators. *Nano Energy* **80**, 105551 (2021).
17. Zhang, B., Lyu, G., Kelly, E. A. & Evans, R. C. Forster resonance energy transfer in luminescent solar concentrators. *Adv. Sci.* **9**, e2201160 (2022).
18. Yu, K. et al. Integration of conjugated copolymers-based luminescent solar concentrators with excellent color rendering and organic photovoltaics for efficiently converting light to electricity. *Adv. Opt. Mater.* **11**, 2202283 (2023).
19. Meinardi, F., Bruni, F. & Brovelli, S. Luminescent solar concentrators for building-integrated photovoltaics. *Nat. Rev. Mater.* **2**, 1–9 (2017).
20. Xia, P. et al. Luminescent solar concentrator with advanced structure for reabsorption loss suppression and synergistic energy harvesting. *Adv. Funct. Mater.* **34**, 2401121 (2024).
21. Xia, P. et al. Luminescent solar concentrators with dual functions of photovoltaic and piezoelectric properties for wireless self-powered speed measurement. *Adv. Energy Mater.* **13**, 2301332 (2023).
22. Xia, P. et al. Glass-compatible and self-powered temperature alarm system by temperature-responsive organic manganese halides via backward energy transfer process. *J. Energy Chem.* **78**, 188–194 (2023).
23. Cho, J. et al. Semitransparent energy-storing functional photovoltaics monolithically integrated with electrochromic supercapacitors. *Adv. Funct. Mater.* **30**, 1909601 (2020).
24. Taşer, A., Kazanasmaz, T., Kundakçı Koyunbaba, B. & Durmuş Arsan, Z. Multi-objective evolutionary optimization of photovoltaic glass for thermal, daylight, and energy consideration. *Sol. Energy* **264**, 112070 (2023).
25. Mustafa, M. N. et al. Smart window technology and its potential for net-zero buildings: a review. *Renew. Sust. Energy Rev.* **181**, 113355 (2023).
26. Bai, T. et al. Dual-band electrochromic smart windows towards building energy conservation. *Sol. Energy Mat. Sol. Cells* **256**, 112320 (2023).
27. Zhou, Y. et al. Unconventional smart windows: materials, structures and designs. *Nano Energy* **90**, 106613 (2021).
28. Li, Q., Wang, B., Zou, H., Guo, Q. & Nie, G. High performance multi-color Prussian blue/poly(indole-5-carboxylic acid) nanocomposites with multiple layer nanosphere structure for electrochromic supercapacitor application. *J. Alloy Compd.* **921**, 166140 (2022).
29. Park, C. et al. High-coloration efficiency and low-power consumption electrochromic film based on multifunctional conducting polymer for large scale smart windows. *ACS Appl. Electron. Mater.* **3**, 4781–4792 (2021).
30. Guo, Q. et al. High performance polythiophene derivative with good electrochromic and energy storage properties electrochemical synthesized in boron trifluoride diethyl etherate. *Dyes Pigments* **220**, 111709 (2023).
31. Cardoso, M. A. et al. Solar spectral management with electrochromic devices including PMMA films doped with biluminescent ionosilicas. *J. Sol Gel Sci. Technol.* **101**, 58–70 (2021).
32. Wu, W. et al. Self-powered and light-adaptable stretchable electrochromic display. *Adv. Energy Mater.* **13**, 2204103 (2023).
33. Wang, J. et al. A bi-functional device for self-powered electrochromic window and self-rechargeable transparent battery applications. *Nat. Commun.* **5**, 4921 (2014).
34. Wang, Y. et al. A fast self-charging and temperature adaptive electrochromic energy storage device. *J. Mater. Chem. A* **10**, 3944–3952 (2022).
35. Kou, Z. et al. Multi-functional electrochromic energy storage smart window powered by CZTSSe solar cell for intelligent managing solar radiation of building. *Sol. Energy Mat. Sol. Cells* **254**, 112273 (2023).
36. Chang, C.-C. et al. A near-infrared photoelectrochromic device with indoor thermal management for self-powered smart windows. *J. Mater. Chem. C* **11**, 13290–13299 (2023).

37. Knight, A. J. & Herz, L. M. Preventing phase segregation in mixed-halide perovskites: a perspective. *Energy Environ. Sci.* **13**, 2024–2046 (2020).
38. Xu, Z. et al. Halogen redox shuttle explains voltage-induced halide redistribution in mixed-halide perovskite devices. *ACS Energy Lett.* **8**, 513–520 (2022).
39. Giuliano, G., Bonasera, A., Arrabito, G. & Pignataro, B. Semi-transparent perovskite solar cells for building integration and tandem photovoltaics: design strategies and challenges. *Sol. RRL* **5**, 2100702 (2021).
40. Guo, W. et al. Multifunctional self-charging electrochromic supercapacitors driven by direct-current triboelectric nanogenerators. *Adv. Funct. Mater.* **31**, 2104348 (2021).
41. Sun, J. et al. Self-powered electrochromic devices with tunable infrared intensity. *Sci. Bull.* **63**, 795–801 (2018).
42. Li, H., Firby, C. J. & Elezzabi, A. Y. Rechargeable aqueous hybrid Zn^{2+}/Al^{3+} electrochromic batteries. *Joule* **3**, 2268–2278 (2019).
43. Zhang, J. et al. Highly conductive $Ti_3C_2T_x$ MXene hybrid fibers for flexible and elastic fiber-shaped supercapacitors. *Small* **15**, e1804732 (2019).
44. Zhang, X. et al. Direct synthesis of porous graphitic carbon sheets grafted on carbon fibers for high-performance supercapacitors. *J. Mater. Chem. A* **7**, 3298–3306 (2019).
45. Mathis, T. S. et al. Energy storage data reporting in perspective-guidelines for interpreting the performance of electrochemical energy storage systems. *Adv. Energy Mater.* **9**, 1902007 (2019).
46. Chen, J. & Lee, P. S. Electrochemical supercapacitors: from mechanism understanding to multifunctional applications. *Adv. Energy Mater.* **11**, 2003311 (2020).
47. Wu, Q. et al. Cyclic stability of supercapacitors: materials, energy storage mechanism, test methods, and device. *J. Mater. Chem. A* **9**, 24094–24147 (2021).
48. Wang, C. et al. A core-sheath holey graphene/graphite composite fiber intercalated with MoS_2 nanosheets for high-performance fiber supercapacitors. *Electrochim. Acta* **305**, 493–501 (2019).
49. Guo, Q., Li, Q., Zheng, L., Xu, X. & Nie, G. Facile preparation of oxygen vacancy $WO_3-X@TiO_2-X$ /poly(indole-6-carboxylic acid) ternary composites with enhanced energy storage capacity and their supercapacitor application. *ACS Appl. Energy Mater.* **5**, 8443–8451 (2022).
50. Guo, Q., Zhao, X., Li, Z., Wang, D. & Nie, G. A novel solid-state electrochromic supercapacitor with high energy storage capacity and cycle stability based on poly(5-formylindole)/ WO_3 honey-combed porous nanocomposites. *Chem. Eng. J.* **384**, 123370 (2020).
51. Sánchez-Romate, X. F. et al. A proof of concept of a structural supercapacitor made of graphene coated woven carbon fibers: EIS study and mechanical performance. *Electrochim. Acta* **370**, 137746 (2021).
52. Ramesh, T., Vedarajan, R., Rajalakshmi, N. & Reddy, L. R. G. Dynamic electrochemical impedance spectroscopy as a rapid screening tool for supercapacitor electrode materials. *J. Mater. Sci. Mater. Electron.* **31**, 1681–1690 (2019).
53. Pinheiro, D. et al. Electrochromic windows based on luminescent acrylate/ionosilicas. *J. Sol Gel Sci. Technol.* <https://doi.org/10.1007/s10971-024-06342-8> (2024).
54. Zhao, Y. & Zhang, X. In situ activation graphitization to fabricate hierarchical porous graphitic carbon for supercapacitor. *Sci. Rep.* **11**, 6825 (2021).
55. Huang, Z.-H. et al. An electro-activated bimetallic zinc-nickel hydroxide cathode for supercapacitor with super-long 140,000 cycle durability. *Nano Energy* **82**, 105727 (2021).
56. Shi, Y. et al. Structure modulated amorphous/crystalline WO_3 nanoporous arrays with superior electrochromic energy storage performance. *Sol. Energy Mat. Sol. Cells* **212**, 110579 (2020).
57. Hu, T. et al. Coupling between cathode and anode in hybrid charge storage. *Joule* **7**, 1176–1205 (2023).
58. Hsu, C.-T., Hu, C.-C., Wu, T.-H., Chen, J.-C. & Rajkumar, M. How the electrochemical reversibility of a battery-type material affects the charge balance and performances of asymmetric supercapacitors. *Electrochim. Acta* **146**, 759–768 (2014).
59. Wu, J. et al. Efficient and stable thin-film luminescent solar concentrators enabled by near-infrared emission perovskite nanocrystals. *Angew. Chem. Int. Edit.* **59**, 7738–7742 (2020).
60. Chen, C. et al. Flexible inorganic $CsPbI_3$ perovskite nanocrystal-PMMA composite films with enhanced stability in air and water for white light-emitting diodes. *Nanotechnology* **31**, 225602 (2020).
61. Protesescu, L. et al. Nanocrystals of cesium lead halide perovskites ($CsPbX_3$, X = Cl, Br, and I): novel optoelectronic materials showing bright emission with wide color gamut. *Nano Lett.* **15**, 3692–3696 (2015).
62. Park, K. et al. Luminescent solar concentrator efficiency enhanced via nearly lossless propagation pathways. *Nat. Photonics* **18**, 177–185 (2024).
63. Luo, X., Ding, T., Liu, X., Liu, Y. & Wu, K. Quantum-cutting luminescent solar concentrators using ytterbium-doped perovskite nanocrystals. *Nano Lett.* **19**, 338–341 (2019).
64. Cai, K. B. et al. Two-dimensional self-assembly of boric acid-functionalized graphene quantum dots: tunable and superior optical properties for efficient eco-friendly luminescent solar concentrators. *ACS Nano* **16**, 3994–4003 (2022).
65. Yang, C. et al. Consensus statement: standardized reporting of power-producing luminescent solar concentrator performance. *Joule* **6**, 8–15 (2022).
66. Yang, C., Liu, D., Bates, M., Barr, M. C. & Lunt, R. R. How to accurately report transparent solar cells. *Joule* **3**, 1803–1809 (2019).

Acknowledgments

C.W. and S.X. acknowledge support from the Natural Science Foundation of China (Grant Nos. 22475043, 22075043, 21875034 and 12274075).

Author contributions

C.W., S.X. and S.H. conceived the idea and designed the experiments. S.H., H.G., P.X. and H.S. conducted the synthesis and characterization. S.H., H.G. and P.X. performed the electrochemical and optoelectronic performance tests. S.H. organized the figures. S.H. wrote the manuscript. C.W., S.X. and S.H. revised the manuscript. J.Z., C.L. (Changgui Lu), Y.F. and C.L. (Cai Liang) supervised the research. All authors contributed to the manuscript preparation.

Competing interests

The authors declare no competing interests.

Additional information

Supplementary information The online version contains supplementary material available at <https://doi.org/10.1038/s41467-025-57369-6>.

Correspondence and requests for materials should be addressed to Shuhong Xu or Chunlei Wang.

Peer review information *Nature Communications* thanks Alice Lee-Sie Eh and the other, anonymous, reviewer(s) for their contribution to the peer review of this work. A peer review file is available.

Reprints and permissions information is available at <http://www.nature.com/reprints>

Publisher's note Springer Nature remains neutral with regard to jurisdictional claims in published maps and institutional affiliations.

Open Access This article is licensed under a Creative Commons Attribution-NonCommercial-NoDerivatives 4.0 International License, which permits any non-commercial use, sharing, distribution and reproduction in any medium or format, as long as you give appropriate credit to the original author(s) and the source, provide a link to the Creative Commons licence, and indicate if you modified the licensed material. You do not have permission under this licence to share adapted material derived from this article or parts of it. The images or other third party material in this article are included in the article's Creative Commons licence, unless indicated otherwise in a credit line to the material. If material is not included in the article's Creative Commons licence and your intended use is not permitted by statutory regulation or exceeds the permitted use, you will need to obtain permission directly from the copyright holder. To view a copy of this licence, visit <http://creativecommons.org/licenses/by-nc-nd/4.0/>.

© The Author(s) 2025